Membrane Anchoring and Ion-Entry Dynamics in P-type ATPase Copper Transport

Grønberg, Christina; Sitsel, Oleg; Lindahl, Erik; Gourdon, Pontus; Andersson, Magnus

Published in:
Biophysical Journal

DOI:
10.1016/j.bpj.2016.10.020

2016

Document Version:
Peer reviewed version (aka post-print)

Membrane anchoring and ion-entry dynamics in P-type ATPase copper transport

C. Grønberg, O. Sitsel, E. Lindahl, P. Gourdon, and M. Andersson

Running title: Cu^{+} ATPase anchoring and dynamics

Keywords: P-type ATPases, membrane transport, metal ion, molecular dynamics simulations

Abstract

Cu^+-specific P-type ATPase membrane protein transporters regulate cellular copper levels. Lack of crystal structures in Cu^+-binding states has limited understanding for how ion entry and binding is achieved. Here, we characterize the molecular basis of Cu^+ entry using molecular dynamics simulations, structural modeling, as well as *in vitro* and *in vivo* functional assays. Protein structural rearrangement resulting in exposure of positive charges to bulk solvent rather than to lipid phosphates proposes a direct molecular role of the putative docking platform for Cu^+ delivery. Simulations in the presence and absence of Cu^+ and mutational analyses predict the ion-entry path to involve two ion-binding sites; one transient Met148-Cys382 site and one intramembranous site formed by trigonal coordination to Cys384, Asn689, and Met717. The results reconcile earlier biochemical and X-ray absorption data and provide a molecular understanding of ion entry in Cu^+-transporting P-type ATPases.

Introduction

Transition metals are critical for a range of cellular processes (1, 2), yet elevated cellular concentrations of these ions are highly toxic (3, 4). Ion homeostasis is maintained by a carefully orchestrated interplay between a set of proteins that mediate transport across membranes (5-7). Breakdown of this machinery results in irregularities in the levels of heavy metals, often with severe physiological effects (8). For instance, a range of mutations in the human Cu^+-transporting class IB P-type (P_{IB-1}) ATPases ATP7A and ATP7B give rise to the severe Menkes' and Wilson's diseases manifested as copper deficiency and overload, respectively (8). The recent crystal structures of a bacterial homologue from *Legionella pneumophila* (LpCopA) (9, 10) and the closely related Zn^{2+}-transporting P_{IB-2}-ATPases (11) have provided a structural framework to understand transition-metal P-type (P_{IB}) ATPase transport and related diseases. However, the Cu^+- and Zn^{2+}-ATPase crystal structures and conserved sequence motifs show significant differences in the intramembranous ion-binding sites (12-16), which suggest that the ion-entry mechanisms and determinants of ion specificity are likely unique to each P-type ATPase heavy-metal transporter. Here, we address the central question how the transported Cu^+ ion is delivered to the protein interior for further ATP-dependent transport.

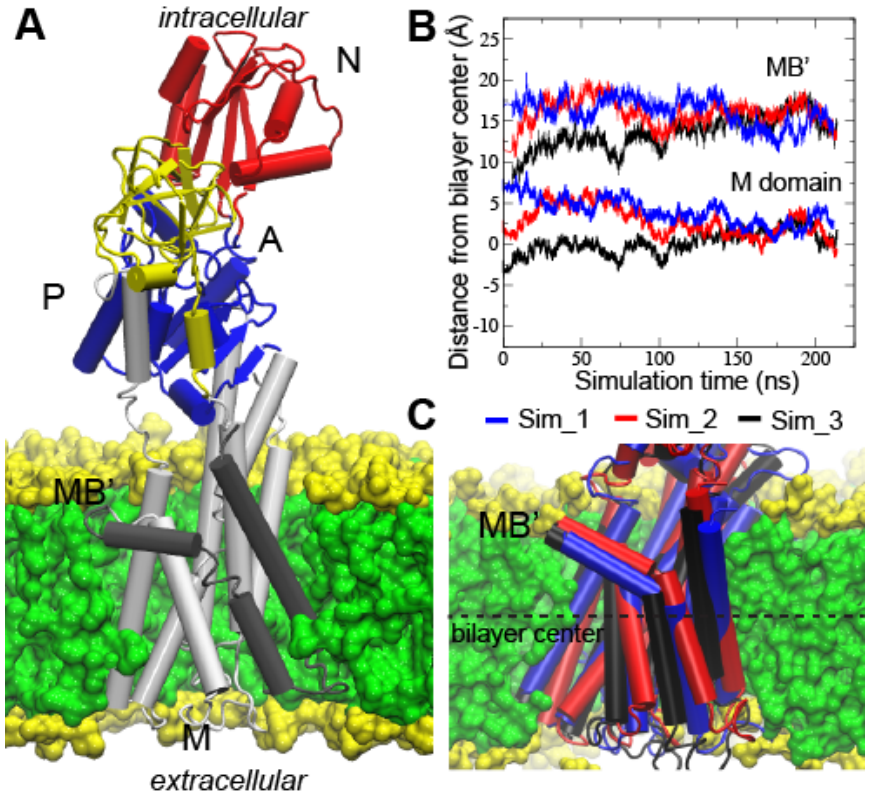

Figure 1. Lipid partitioning of the LpCopA membrane domain. **(A)** The LpCopA E2.P_i crystal structure (PDB ID: 3RFU) inserted into a DOPC lipid bilayer with the acyl-chain and polar head group regions shown in green and yellow, respectively. The soluble N, P and A cytoplasmic soluble domains are colored red, blue, and yellow, respectively. The P_{IB}-ATPase specific and P-type ATPase common TM helices in the membrane M domain are shown in gray and white, respectively. **(B)** The center-of-mass (COM) for the M-domain and MB' helix, respectively, for the three Cu^+-free E2.P_i simulations. **(C)** The average structures corresponding to > 150 ns displaying the docked positions in the membrane.

All P-type ATPase proteins share a common structural core of intracellular A- (actuator), P- (phosphorylation) and N- (nucleotide binding) cytosolic domains and a TM (transmembrane) domain

(17) (Fig. 1A). The Post-Albers [E1]-[E1P]-[E2P]-[E2] scheme (P denotes phosphorylated) is used to describe four structurally distinct reaction intermediate cornerstones associated with P-type ATPase-mediated transport (18, 19) (Fig. S1 in the Supporting Material). Here, E1 and E2P denote states in which the TM domains are open towards the cytoplasm and non-cytoplasmic space, respectively. Conformational changes associated with autophosphorylation (from E1 to E1P) and autodephosphorylation (E2P to E2) in the A-, P- and N-domains are coupled to changes in accessibility to intramembranous ion-binding residues in the TM portion of the protein, which results in ion transport (16). Additionally, intermediate states other than the cornerstone [E1]-[E1P]-[E2P]-[E2] occur during the transport cycle of P-type ATPases and have been extensively described elsewhere (20). Interestingly, the heavy-metal P_{IB}-ATPases also contain two N-terminal class IB-specific structural features; the TM helices denoted MA and MB in addition to TM helices M1-M6 present in all P-type ATPases, and an N-terminal heavy-metal binding domain (HMBD). Furthermore, a combined crystallography/computational approach recently indicated that the P_{IB}-specific TM helices contribute to a Cu^+-release pathway regulated by unique structural rearrangements (10). In contrast, the HMBD binds metal ions but seems not to be strictly required for ion translocation, which suggests a regulatory function (9, 21, 22).

Soluble chaperone proteins coordinate Cu^+ to maintain very low intracellular concentrations and are responsible for supplying ions to Cu^+-ATPases for subsequent extrusion (23). CopZ chaperones have been shown to deliver Cu^+ to the TM domain of *Archaeoglobus fulgidus* CopA (AfCopA), while the HMBD lacked such capability (21). Based on the LpCopA crystal structures, the C-terminal part of helix MB (referred to as MB') was assigned a putative role as docking platform for such chaperones (9). In agreement with this notion, mutations of an electronegative patch of a CopZ chaperone

abolished Cu^+ transport in AfCopA (24), which suggests positively charged amino acids on the MB' helix to be the target for chaperone interactions with the surface of the protein core. In the docked position, the chaperone Cu^+-binding site is presumably located close to the putative initial Cu^+ receivers Met148, Glu205, and Asp337 (residue numbers refer to LpCopA throughout), as observed for Ca^{2+} in the related Ca^{2+}-transporting P-type ATPase SERCA1a (9, 25). In SERCA1a, the ions are then transferred to two internal Ca^{2+}-binding sites (26, 27), but the exact number, location, and chemical nature of the entry pathway in CopA proteins are unknown because the available structural information is limited to E2 states (9, 10), where copper already has been deposited to the non-cytosolic side. Mutagenesis and copper binding experiments have suggested two intramembranous ion-binding sites for AfCopA formed by a set of invariant residues (Site I: Cys382, Cys384 and Tyr688, and Site II: Tyr688, Asn689, Met717 and Ser721) (16). Similarly, a two-ion stoichiometry per protein was also observed in plant Cu^+ ATPases (28). However, a recent report for LpCopA rather indicated a combination of a transient site, partially exposed to the cytoplasmic membrane-water interface and a subsequent single transmembrane high-affinity metal-binding site (14). While the critical residues are similar in-between the enzymes in agreement with the notion of a common Cu^+ ATPase transport mechanism, significant alterations are found in the respective HMBD and consequently it cannot be excluded that these or subtle changes in the TM domain contribute to the observed differences in distinct metal sites. Structural information from X-ray absorption experiments proposed the high-affinity site in LpCopA to coordinate Cu^+ in a trigonal sulfur-only site consisting of residues Cys382, Cys384, and Met717 (14). Therefore, residues Asn689 and Ser721 appear unlikely to constitute stable Cu^+ ligands in LpCopA, although a more transient role in trafficking of the ion cannot be excluded.

Hence, while the overall structural features involved in Cu^+ entry have been sketched out, the molecular details are still missing. Furthermore, because crystal structures are trapped within a static lattice and typically do not contain structural information on the surrounding lipid bilayer, alternative methods are needed to understand the dynamical features involved in Cu^+ membrane transport. Molecular dynamics (MD) simulations can describe structural dynamics of a protein embedded in a lipid environment under physiological conditions and therefore enables a unique atomistic view of membrane protein transport. However, parameterization of force fields will introduce uncertainties, in particular when describing metal-ion interactions. In addition, enhanced sampling techniques often need to be introduced to enable simulation of biological events, such as ions entering a protein. Therefore, it is critical to verify the theoretical predictions with experimental data, such as the *in vitro* and *in vivo* mutational activity studies used in this work.

Here, we characterized the proposed MB' docking platform and Cu^+ entry mechanism in LpCopA embedded in a membrane environment using MD simulation techniques and mutational activity assays. Partitioning of the LpCopA protein in the membrane resulted in a reorientation of the amphipathic MB' helix relative to the crystal structure that exposed positively charged side chains of Lys135, Lys142 and in particular Arg136 side chains to the surrounding bulk solvent, providing "antennas" that may guide the docking of a negatively charged HMBD and/or copper-delivering chaperones. *In vitro* and *in vivo* activity measurements confirmed the functional importance of these positive charges. Of the three proposed entry site residues, Met148 showed significant flexibility towards the internal Cys382 in simulations of the $E2.P_i$ structure, and the Met148-Cys382 residue pair constituted components of a transient binding site in simulations in the presence of Cu^+ ions in an E1 structural homology model. Several Met148 mutants showed impaired activities both *in vitro* and *in vivo* establishing Met148 as the

mediator of ion transfer between the entry and high-affinity binding sites. Furthermore, the E1 simulations suggest that Cys382 is relaying Cu^+ to a single high-affinity binding site, formed by residues Cys384, Asn689, and M717, which refine recent biophysical observations.

Materials and Methods

Building and simulation of the Cu^+-free systems

The crystal structure of the copper-transporting class IB P-type ATPase lpg1024 (LpCopA) from *Legionella pneumophila* trapped in an E2.P_i state (PDB ID: 3RFU) (9) was used as starting structure for the Cu^+-free MD simulations. The protein was inserted into a lipid bilayer consisting of 550 DOPC lipid molecules built using the CHARMM-GUI membrane builder (29). Three positions of the protein with respect to the vertical z-axis of the membrane were chosen; the position predicted by the "Orientation of Proteins in Membranes" (OPM) database (30) (Sim_2), 5 Å below (-z) the OPM position (Sim_1), and 5 Å above (+z) the OPM position (Sim_3) (Fig. S2 in the Supporting Material). Lipids within 0.6 Å of the protein (25 lipids on each leaflet) were removed to avoid protein-lipid steric clashes. After solvation by 77,637 water molecules and addition of 7 Na^+ counter-ions to achieve electrical neutrality, each system consisted of a total of 311,957 atoms.

Three independent >200 ns atomistic MD simulations were performed. Each simulation system was relaxed using a 10,000-step of conjugate-gradient energy minimization followed by gradual heating, from 0 to 310 K over 120 ps. Equilibrated positions of lipids and water molecules were obtained by two consecutive 1 ns simulations at constant temperature (310 K) and volume (NVT ensemble), where the harmonical restraints of these groups were released successively. The protein was then progressively released from its initial configuration over seven 1 ns simulations, followed by a

production run at constant temperature (310 K) and pressure (1 atm) (NPT ensemble). The MD simulations were run with the NAMD 2.9 software package (31). The CHARMM22 including CMAP correction (32) and CHARMM36 (33) force fields were used for protein and lipids, respectively, and the TIP3P model (34) was used for the water molecules. We note that the new CHARMM36 protein force field (35) resulted in very similar simulated molecular dynamics during a 35 ns control run (Fig. S3 in the Supporting Material). In addition, the CHARMM36 force field is expected to affect protein folding (e.g. helicity) rather than the protein-lipid, protein-water interactions and side-chain dynamics investigated here. A time step of 1 fs was used to integrate the equations of motion, and a reversible multiple time step algorithm of 4 fs was used for the electrostatic forces and 2 fs for short-range, non-bonded forces. The smooth particle mesh Ewald method (36, 37) was used to calculate electrostatic interactions. The short-range interactions were cut off at 12 Å. All bond lengths involving hydrogen atoms were held fixed using the SHAKE (38) and SETTLE (39) algorithms. A Langevin dynamics scheme was used for thermostating and Nosé-Hoover-Langevin pistons were used for pressure control (40, 41).

Building and simulation of the Cu^+ systems

Biochemical and structural studies suggest that the overall conformational changes of P-type ATPases are well-conserved (20, 42). As a consequence, individual soluble A-, N- and P-domains of zinc- and copper-transporting P_{IB}-ATPases superimpose almost perfectly with the corresponding calcium-pumping P_{IIA}-ATPase states, and the same holds true for sodium/potassium and proton transporters (P_{IIC}- and P_{IIIA}-ATPases). Therefore, the E1 LpCopA model was built based on the high-resolution E2P structure of LpCopA (PDB ID: 4BBJ) (10) and a SERCA1a E1 crystal structure (PDB ID: 4H1W) (25) as template using the software Coot (43). First, the soluble A-, P- and N-domains of 4BBJ and 4H1W

were aligned using secondary structure-matching (SSM) superpositioning (44). The resulting positions of the A- and P-domains were then used as anchoring points for the second SSM procedure, positioning TM helices M2 and M3 as well as M4 and M5, which then functioned as anchors for placement of M1 and M6 in a third SSM superpositioning. Finally, TM helices MA and MB were placed in similar positions relative to M1 as observed in 4BBJ (with 4BBJ and the E1 model aligned on M1 and M2 using SSM). The connecting linkers of the soluble domains were modeled using a similar SSM approach. In contrast, the short connecting loops between the TM helices were maintained as in the structurally determined E2 states of LpCopA.

To construct a new simulation system for modeling Cu^+ interactions, we superimposed the E1 model onto an average structure corresponding to the equilibrated (>150 ns) part of the Sim_2 trajectory and 12 lipids within 0.5 Å from the protein were removed to avoid clashes. This was followed by a 10,000 step conjugate gradient energy minimization and a short 10 ns using CHARMM22 and CHARMM36 force fields for protein and lipids, respectively (32, 33), with backbone restraints to equilibrate lipids around the protein. We now considered this system a good starting point for a new, independent simulation addressing Cu^+ interactions, and therefore converted the atoms to be consistent with the ffGromos53a6 force field, which contains Cu^+ parameters (45), by renaming atom types and deleting undefined protein and lipid hydrogens. Water molecules were described by the simple point charge (SPC) water model (46). To initiate this new simulation, we first performed a 50,000 step steepest descent energy minimization, followed by a 100 ps and 100 ns equilibration in the NVT and NPT ensembles, respectively, with backbone restraints to equilibrate lipid and water interactions, as well as side-chain configurations while maintaining the modeled E1 state. The Ramachandran plots of the 4BBJ crystal structure and equilibrated E1 model were more or less identical (Fig. S4 in the Supporting

Material). A Cu^+ ion was positioned 2.5 Å from residue E205, which has been assigned a putative role in ion entry and is located above the formed water cavity. Following equilibration, the GROMACS pull code (47) with a 1,000 kJ mol^{-1} nm^{-2} force constant was applied on Cu^+ in the *z* dimension directed toward the extracellular side. In two separate simulations, pull rates of 1.25 and 2.5 Å/ns were applied for 10 and 5 ns, respectively with the protein backbone atoms as reference. Ramachandran plots before and after the pull showed minor perturbation to the structure (Fig. S4). A 2 fs time step was used, and short-range non-bonded interactions were cut off at 1.4 nm, with long-range electrostatics calculated with the particle mesh Ewald (PME) algorithm (36, 37). The temperature of the system was maintained by separate coupling of the protein and non-protein atoms to external temperature baths at 310 K with a Nose–Hoover thermostat (48, 49), and the Parrinello–Rahman barostat (50, 51) was used to isotropically regulate pressure. All bond-lengths in the protein were constrained with the LINCS algorithm (52). In the two-ion simulations, pull code protocols were applied in identical fashion as for the single Cu^+ ion trajectories, except with binding Cu^+ ion positioned either in the transient entry site or the internal binding site.

Computational analyses

Molecular graphics and simulation analyses were generated with the VMD 1.9.1 software package (53). All alignments between different CopA structures were based on the TM region defined by residues 74 – 203 (TM helices MA-M2), 335 – 390 (M3-M4) and 679 – 730 (M5-M6). The MB' helix was defined as residues 129-144. The criteria for the MB' residue interactions to either water, lipid carbonyl oxygens or lipid phosphates were 3.5 Å distance and 40 degree angles, while Cu^+ interactions were set to protein residues within 3.5 Å.

Protein Expression and Purification

The overproduction and purification of LpCopA is described in Gourdon et al. (9). Briefly, the recombinant protein was overproduced in *E. coli* followed by cell lysis in a high-pressure homogenizer. The membranes were isolated and solubilized with $C_{12}E_8$ at a final concentration of 18.6 mM. The LpCopA protein was subsequently purified by nickel affinity and size-exclusion chromatography.

***In vitro* characterization**

The Baginski method with arsenic detection under aerated conditions was used to monitor ATPase activity (54). The reaction mixture contained 4 μM LpCopA, 40 mM MOPS-KOH pH=6.8, 150 mM NaCl, 5 mM KCl, 5 mM $MgCl_2$, 20 mM $(NH4)_2SO_4$, 20 mM L-cysteine, 5 mM NaN_3, 0.25 mM Na_2MoO_4, 1.2 mg/ml L-α-phosphatidylcholine lipids from soybean extract, and 3.7 mM $C_{12}E_8$ in a total volume of 50 μL. To prevent activity from background copper and silver contaminants, 10 μM ammonium tetrathiomolybdate was added followed by incubation for 15 minutes with 1 mM $CuCl_2$ (reduced to Cu^+ by the cysteine present in the sample). Reactions were started by addition of 5 mM ATP followed by incubation at 120 rpm for 25 minutes at 37 °C and stopped by adding 50 μL of freshly made stop-solution containing 0.1 % sodium dodecyl sulfate (SDS), 0.4 M HCl, 0.14 mM L-ascorbic acid, and 4.7 mM $(NH_4)_6Mo_7O_{24}•4H_2O$. After 10 minutes of incubation at 19 °C, 75 μL stabilizing solution (15 mM $NaAsO_2$, 70 mM $Na_3C_6H_5O_7•2H_2O$, 350 mM CH_3COOH) was added and followed by a final 30 minute incubation at 19 °C and absorbance measured at 860 nm. To allow comparison of wild-type and mutant LpCopA activities the relative protein concentrations were determined by quantification and comparison of individual SDS-PAGE band intensities using ImageJ (55). A second SDS-PAGE gel was generated with roughly equal protein amounts, as calculated from

the first gel (Fig. S5 in the Supporting Material) and the protein amounts were re-quantified by ImageJ and information on the variation between these amounts was then used to scale the results of the Baginski assay accordingly. The protein concentration of the D426N mutant was determined with light absorbance at 280 nm and used as reference in the activity assay. These data were normalized to 0-100% according to activities of the LpCopA D426N dead mutant (or no protein) and the wild-type proteins, respectively. Each reported measurement was based on nine replicates.

In vivo characterization

The CopA-deleted *E. coli* strain CN2328, its progenitor strain CN1709, and the plasmid pCN2345 containing the native *E. coli* CopA promoter and gene were obtained from Lisbeth Birk Møller (56). As reported previously (10), the pCN2345 plasmid was mutated to allow LpCopA wild-type or mutant genes to replace the *E. coli* CopA gene, while preserving the native *E. coli* CopA promoter. The plasmids were transformed into CN2328 cells and an empty pET22b(+) vector was transformed into CN1709 cells and used as a control. Pre-cultures were grown overnight and their OD_{600nm} were adjusted to 1.0 and 10 µL cell culture was used to inoculate 190 µl of LB media containing 100 µg/mL ampicillin and the $CuCl_2$ concentrations were adjusted to 0 and 3.5 mM. The inoculated media were grown in 96-well plates at 200 rpm and 37 °C and OD_{560nm} was measured in hourly intervals. The OD_{560nm} of cells grown in 3.5 mM $CuCl_2$ for 309 minutes is shown in Fig. S6 in the Supporting Material. Each reported measurement was based on three replicates.

Results

Lipid partitioning of the Cu^+ ATPase membrane domain

When sampling structural dynamics of membrane proteins using MD techniques the protein needs to be

embedded in a lipid environment. Traditionally, the initial position of the TM domain with respect to the surrounding lipid bilayer is achieved by identification of membrane-spanning helices and subsequent alignment to the lipid bilayer center-of-mass (COM). Because crystal structures typically do not provide information on the lipid bilayer boundaries, definition of TM helices becomes somewhat speculative. The "Orientation of Proteins in Membranes" (OPM) database (30) utilize transfer energy minimization between water and the membrane to predict the docking of the membrane-spanning parts into lipid bilayers. Because our study investigates the structural environment involved in ions entering into the TM domain, a well-equilibrated position of the protein with respect to the membrane is critical. Therefore, to search for the optimal location of the putative MB' ion docking platform in the membrane-water interface, the partitioning process was monitored by comparing three atomistic simulations of the LpCopA; one in which the TM region was aligned with the membrane according to predictions from the OPM database, and two additional simulations where the protein TM COM was either 5 Å above or below the aligned position (Sim_1, Sim_2, Sim_3; see Fig. S2 and Table S1). The partitioning process was considered to have reached convergence at 150 ns by means of tracking the COM for the TM domain and the MB' helix for each system (Fig. 1B). In principle, a set of independent simulations that fulfill a criterion of convergence (such as COM alignment in the z-dimension) should report similar structural properties (such as internal water density). To test this, the water density profiles across the lipid bilayer were calculated for the converged parts (>150 ns) of the three trajectories, and the overall similarity of the obtained profiles validated the convergence assumption (Fig. S7A in the Supporting Material) and therefore the three average structures from >150 ns can be considered equal and equilibrated (Fig. 1C). We compared the protein insertion position achieved by our atomistic simulation protocol to a recent database MemProtMD (57) that relies on a coarse-grained MD simulation lipid partitioning protocol, and observed very similar results (Fig. S7B).

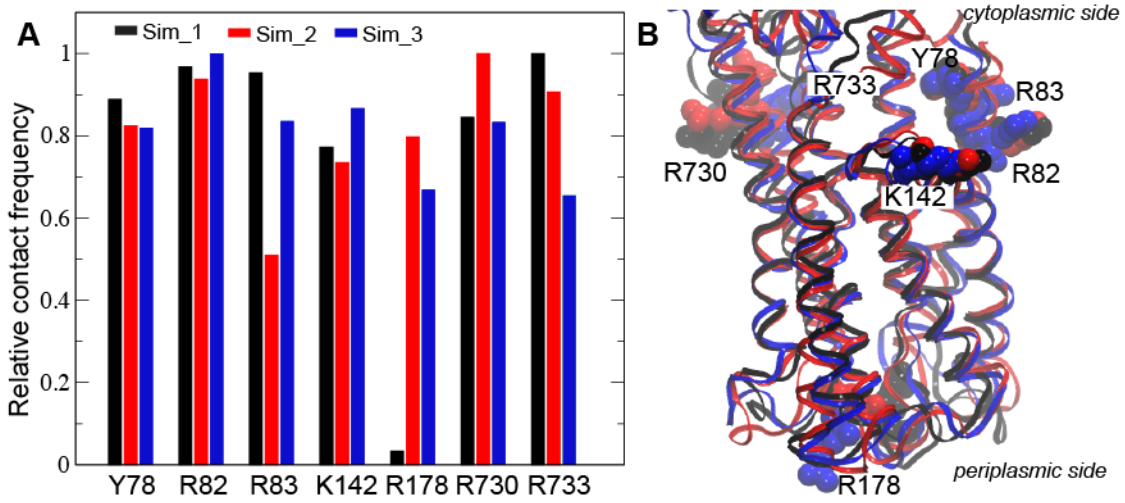

Figure 2. The lipid partitioning of the membrane domain. **(A)** Relative contact frequency of interactions < 2 Å in-between amino acid side chains and lipid phosphates in the three Cu^{+}-free E2.P_i simulations. **(B)** The identified lipid-interacting residues colored according to simulations 1-3 and displayed on the respective averages from > 150 ns.

To determine the key amino acids in anchoring the membrane domain to the lipid bilayer, we tracked all amino acid residues within 2 Å from a lipid phosphate during the equilibrated part in each of the trajectories (>150 ns). The seven most prominent lipid-interacting residues were common in-between trajectories (Fig. 2A), which confirms that the simulated lipid partitioning process is equilibrated. Interestingly, almost all residues showing tight interactions to the surrounding lipids were situated on the cytoplasmic side (Fig. 2B). The exception was the periplasmic residue Arg178, which was registered as highly interacting only in two of the trajectories. The anchoring residues contained one residue located on the putative MB' docking platform, Lys142. These results suggest that membrane docking of the LpCopA protein is achieved by almost exclusively cytoplasmic residues, which may

reflect higher demands of a carefully defined lipid-protein-water interface on the cytoplasmic side, where ion uptake takes place, compared to the periplasmic side.

Exposed positive charges are important for copper transport

Because the MB' platform has been assigned a putative central role in Cu^{+}-delivery at the cytoplasmic membrane interface, we monitored the structural dynamics displayed by this structural component in the lipid environment. Interestingly, the simulated structure showed a significant structural shift in MB' relative to the original crystal structure (Fig. 3A).

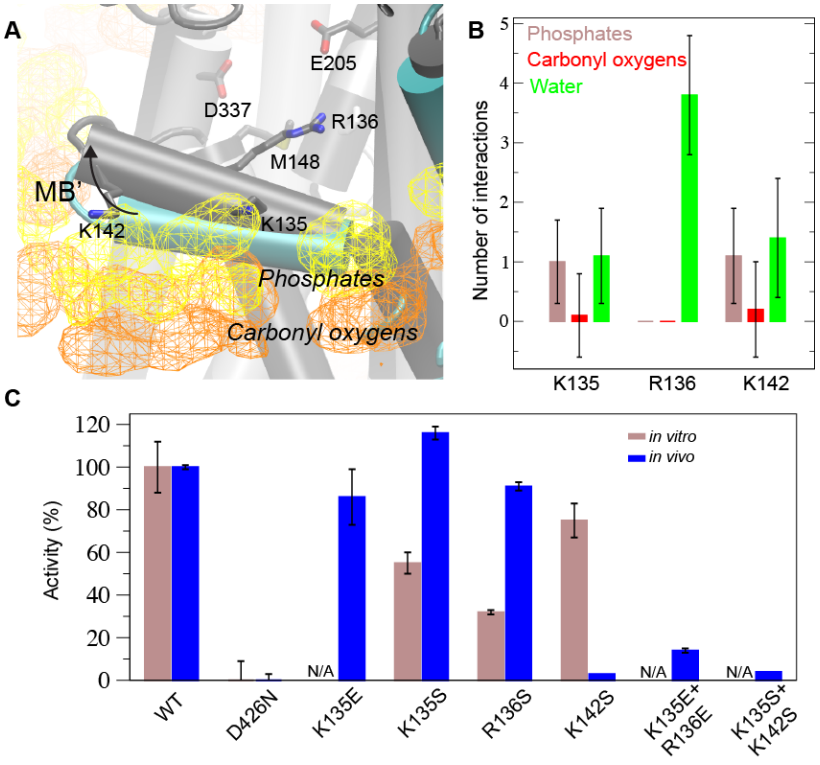

Figure 3. The chemical environment of the putative MB' platform. **(A)** The LpCopA E2.P_i structure and average protein structure representing >150 ns simulation time are shown in cyan and gray, respectively. Isodensity surfaces at 5% occupancy are shown for lipid phosphates and carbonyl

oxygens in yellow and orange, respectively. **(B)** The number of interactions between Lys135, Arg136, Lys142 and lipid phosphates, carbonyl oxygens and water molecules, respectively, from the three E2.P_i simulations. **(C)** Relative *in vitro* (gray) and *in vivo* (blue) activities of LpCopA MB' mutants as compared to wild-type (WT) protein and the inactive Asp426Asn mutant.

This structural rearrangement suggested an increased cytoplasmic exposure of all the docking platform positive charges (Lys135, Arg136, Lys142) relative to the calculated isodensity surfaces corresponding to lipid phosphates and carbonyl oxygens in the equilibrated (>150 ns) portion of the trajectory (Fig. 3A). Because positively charged amino acid residues at the membrane interface are frequently forming strong interactions as membrane anchors with negatively charged lipid phosphate groups (58), exposed positive charges might be indicative of functional roles. We therefore quantified the interactions of the MB' positive charges to lipid phosphates, lipid carbonyl oxygens, and water molecules in the three trajectories. Indeed, residues Lys135, Arg136, and Lys142 showed significant exposure to bulk water molecules, in particular Arg136 that made no specific lipid interactions (Fig. 3B). The overall prediction is therefore that the putative MB' docking platform is characterized by significant exposure of positive charges, in agreement with a charged-based mechanism of chaperone and/or HMBD docking to the MB' platform.

To probe the importance of positive charges on the MB' half-helix, we characterized a set of single and double mutants using *in vitro* and *in vivo* activity assays (Fig. 3C). Inorganic phosphate generated by ATPase turnover by the purified LpCopA protein in lipid-detergent solution was used as a proxy for *in vitro* activity. The *in vivo* activity was assessed by copper resistance of wild-type and mutant LpCopA

forms under control of a native *E. coli* CopA promoter in a CopA-deficient *E. coli* strain. In both assays, the activity was plotted on a scale of 0-100 % defined by the catalytically inactive Asp426Asn mutant and wild-type protein activity, respectively. First, we assessed single-residue charges by individually mutating each charged residue Lys135, Arg136, and Lys142 to a serine. The measured *in vitro* activities were significantly reduced, in particular Arg136Ser that only achieved 32 % of the wild-type activity. This corroborates with the findings from the simulations where Arg136 were fully solvated in all three trajectories, while Lys135 and Lys142 both interacted with surrounding lipids to some extent. However, when probing activity in a biological context the Lys135Ser and Arg136Ser mutants displayed unaffected growth rates under copper stress, whereas Lys142Ser cells showed almost no growth. The observed differences may arise from complex compensatory effects, such as partial mutant protein production to ensure cell survival, differences in membrane composition, protein stability, or combinations of these factors. Furthermore, we note that no copper-delivering chaperone has been identified for LpCopA, or in *E. coli*. Therefore, Cu^{+} ions in the *in vivo* system might be delivered by the HMBD, a hitherto unknown chaperone, or alternative delivery system. The effect of quenching charges on MB' was cumulative since the Lys135Ser+Lys142Ser double mutant showed almost no activity *in vivo*. In addition to characterizing absent charge, we also introduced glutamic acid mutations to probe for responses to charge reversal. Compared to the Ser-substitution, the Lys135Glu mutant displayed a somewhat reduced *in vivo* activity. An additional reversed charge in the Lys135Glu+Arg136Glu double mutant again showed a cumulative reduction of *in vivo* activity. Together, these activity measurements highlight the importance of positive charges on the MB' docking platform in both *in vitro* and *in vivo* settings.

Side-chain dynamics in the putative ion-entry site suggest a Cu^{+} transport pathway

A putative entry site has been assigned to the conserved residues Met148, Glu205 and Asp337, which are located at the cytoplasmic membrane interface (Fig. 4A).

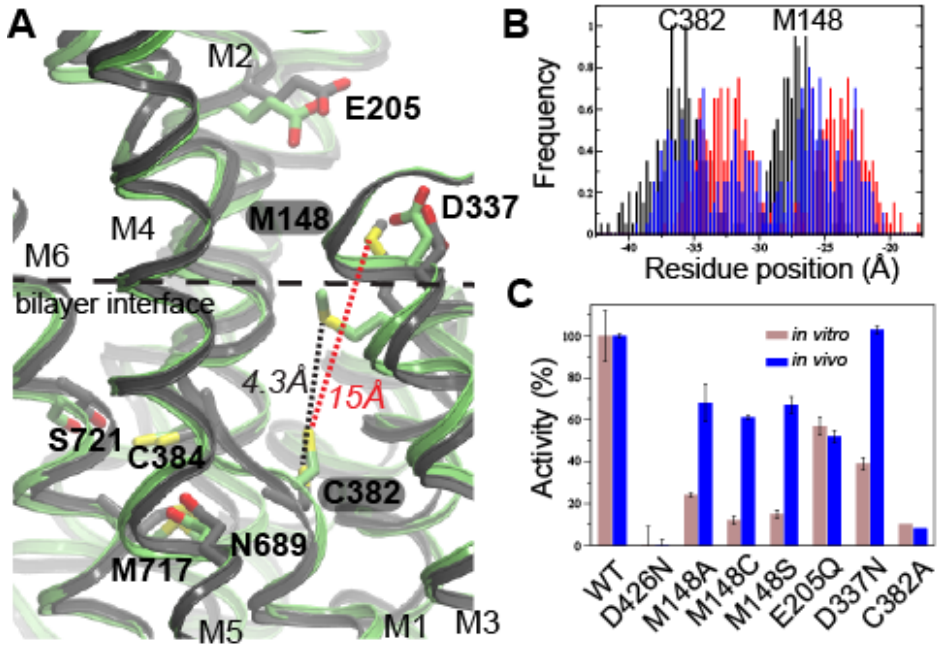

Figure 4. Structural dynamics in the proposed copper entry site. **(A)** The dynamic side-chain reorientation between ion entry site Met148 and the internal ion acceptor Cys382 visualized by two superimposed structures that represent extreme configurations with respect to the Cys382-Met148 distance. The structures with the minimal (4.3 Å) and maximal (15 Å) Met148 - Cys382 distances are represented in green and black, respectively. **(B)** The simulated variations in center-of-mass of residues Met148 and Cys382 in the three Cu^{+}-free simulations; Sim_1 (blue), Sim_2 (red), and Sim_3 (black). **(C)** Relative *in vitro* (gray) and *in vivo* (blue) activities of LpCopA entry/transition site mutants as compared to wild-type (WT) protein and the inactive Asp426Asn mutant.

Cys382, on the other hand, belongs to the proposed internal ion-coordinating residues, and this is the residue most likely to first accept Cu^+ from the entry site due to the proximal location of its copper-binding sulfur atom to the cytoplasm. Therefore, in order to identify residues possibly involved in ion passage from the entry site into the membrane domain, we measured how the simulated distances between the three entry site residues and Cys382 changed relative to the distances in the $E2.P_i$ structure. The minimal distance to the Cu^+ acceptor Cys382 was significantly lower for Met148 compared to residues Glu205 and Asp337 (Fig. S8 in the Supporting Material). In addition, the Met148-Cys382 distance was highly dynamic and varied within an 11 Å range (Fig. S8) corresponding to inter-residue distances between 15 and 4.3 Å (Fig. 4A), where the latter would in principle allow direct copper transfer. However, the average sulfur-to-sulfur Met148-Cys382 distance of 9±2 Å is in agreement with major conformational changes being required for copper transfer from the copper entry site to the high-affinity binding residues as anticipated from the Post-Albers cycle (Fig. 4B and Table S1).

To test the predicted importance of the Met148-C382 interplay, we again performed *in vitro* and *in vivo* mutational analyses (Fig. 4C). Strikingly, Met148Ala, Met148Cys, and Met148Ser mutants displayed a significantly impaired transport capability *in vitro* in agreement with previous indications on the functional role of Met148 (14). The effect was similar to the activity reduction in the Ala mutation of Cys382, the closest high-affinity site residue to the entry site. To test whether this also was true in a cellular environment, we assayed the mutant activities *in vivo* and observed a 40 % reduction in growth rate. However, while the Asp337Asn and Glu205Gln mutants also showed a reduction of the *in vitro* activities, it was less pronounced compared to the Met148 mutations. In addition, while Glu205Gln approximately halved the protein *in vivo* activity, the Asp337Asn mutant showed no observable

impairment. These observations support an important functional role of Met148, most likely in the early stages of metal transfer to the protein, while Glu205 and, in particular, Asp337 seem to be less important (as also underscored by their distal location to Cys382).

A putative Cu^+ entry mechanism

To further characterize the molecular basis of copper transfer to the high-affinity binding residues, access to structural information of reaction cycle states associated with copper uptake and hence open to the cytoplasm will be necessary. In the lack of crystal structures, we turned to modeling based on structural homology. An LpCopA E1 model was constructed by applying similar E2P-to-E1 conformational changes as observed in SERCA1a (PDB IDs: 4H1W (25) and 3B9B (59), respectively) to the LpCopA E2P crystal structure (PDB ID: 4BBJ) (10). The strict conservation of conformational changes in the A-, P- and N-domains observed in all available P-type ATPase crystal structures enables this modeling approach.

During equilibration of the LpCopA E1 model, water molecules entered into a cytoplasmic cavity that extended towards internal amino acid residues proposed to participate in ion binding (14, 16), which is in accordance with an E1 state exposing its internal binding site to the cytoplasm (Fig. S9A in the Supporting Material). The Cu^+ ion was placed 2.5 Å from the putative entry site residue Glu205, which showed enhanced sensitivity compared Asp337 in our functional analyses, and a force directed towards the extracellular side was applied on the ion. In two separate simulations, pull rates of 1.25 and 2.5 Å/ns were applied for 10 and 5 ns (referred to as pull_1 and pull_2, respectively) resulting in ~12.5 Å moves along the membrane vertical (Fig. 5).

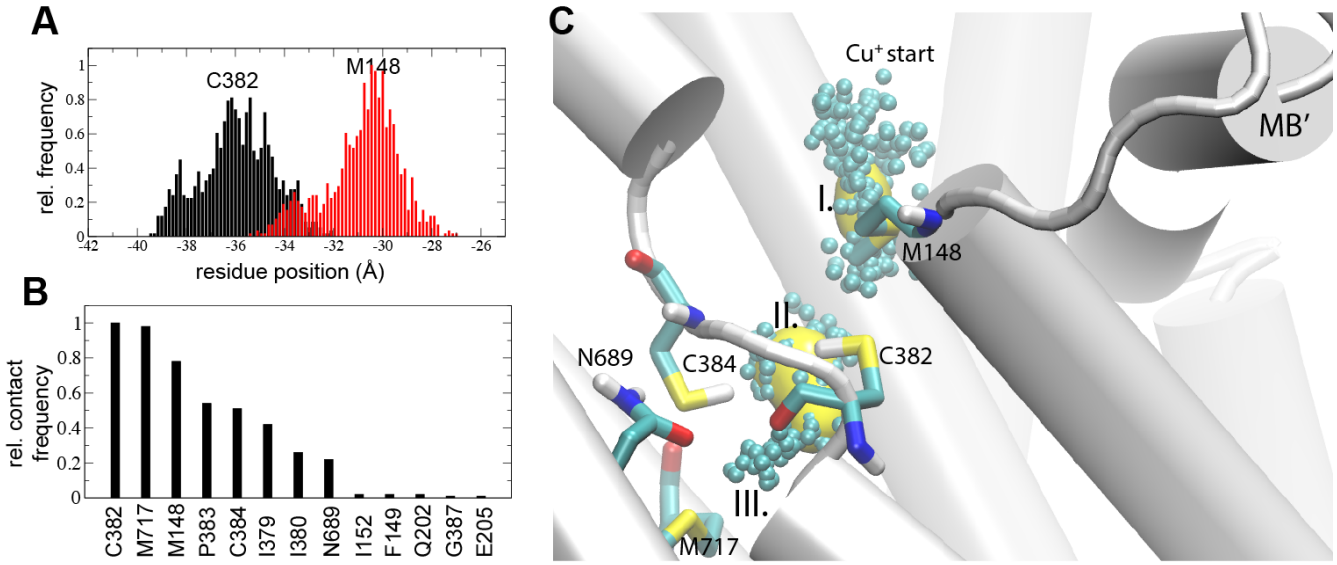

Figure 5. Simulated copper-entry dynamics in the pull_1 simulation. **(A)** Structural rearrangements of Met148 and Cys382 side chains in the presence of Cu^+ depicted as center-of-mass (COM) fluctuations. **(B)** Contact analysis showing the relative number of instances the Cu^+ was < 3.5 Å from any protein residue. **(C)** Copper ions (cyan) extracted from the simulation with preferred Cu^+ positions shown as a yellow isodensity surface at 40% occupancy (Sites I and II). Site III marks the end of the ion pathway.

In both cases, the Cu^+ ion did not engage in protein interactions until it reached Met148. The Cu^+ ion maintained its interaction to Met148 whilst entering into the water-filled cytoplasmic opening in the modeled E1 state (red, transparent isodensity surface in Fig. S9A) and Met148 subsequently shuttled the Cu^+ ion towards Cys382, which was observed to be the primary ion acceptor, thereby confirming the prediction from the Cu^+-free simulations. The average sulfur-to-sulfur distance between Met148 and Cys382 was 5±1 Å in both simulations (Fig. 5A, S9B, and Table S1), which is 4 Å shorter compared to the Cu^+-free simulations. In addition, the minimum Met148-Cys382 inter-residue distance

reached ~3 Å at several instances, which is in agreement with facilitated copper transfer to Cys382 in the E1 state (Fig. S8).

To further characterize the entry-path dynamics, we calculated contact frequencies of residues within 3.5 Å of the Cu^+ ion. Here, we focus on the results from slower pull since increased sampling along the putative pathway better discriminates between the amino acid contributions. The residues Cys382, Met717, and Met148 generated the highest scores in the contact analyses, which confirms Met148 as the primary Cu^+ acceptor and Cys382 as the component that enables shuttling into the protein interior (Fig. 5B). To further refine preferred ion locations along this putative entry pathway, we calculated an isodensity map for the Cu^+ ion in the pull_1 simulation and observed two major high-density regions; one at Met148 (referred to as Site I) and the other in-between Cys382 and Cys384 (referred to as Site II) (Fig. 5C). We observed the ion coming to a halt when encountering Met717 (referred to as Site III), which corroborates with its assigned role as internal ion-binding residue (16). The faster pull rate reproduced these overall results (Fig. S9). In both simulations, the Cu^+ ion was transiently coordinated in-between Met148 and Cys382 (Fig. 6A) after which it was shuttled into the internal ion-binding site consisting of residues Met717, Cys384, and Asn689, which bind Cu^+ with trigonal coordination (Fig. 6B). Noteworthy, the adjacent, invariant and functionally important residues Tyr688 and Ser721 did not partake in copper binding in agreement with recent biophysical measurements (14).

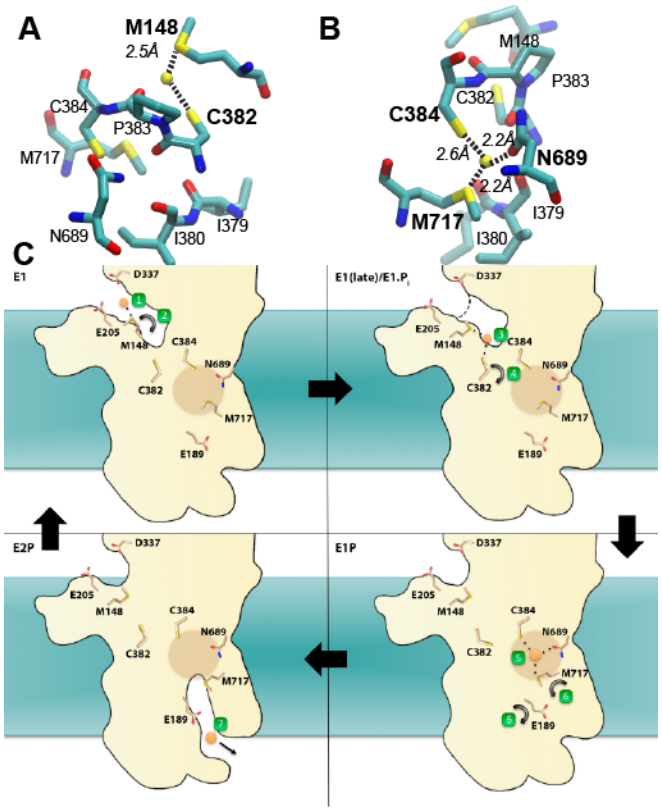

Figure 6. Proposed copper entry and binding mechanism. **(A)** Representative snapshot showing Cu^{+} shuttling between Met148 and Cys382. **(B)** Representative snapshot displaying Cu^{+} binding to the putative internal binding site comprising residues Asn689, Cys384, and Met717. **(C)** Schematic describing the proposed structural basis for Cu^{+} transport.

Finally, we then used a similar protocol to simulate the entry of a second Cu^{+} ion with either the transient (Fig. S9A in the Supporting Material) or the internal (Fig. S9B) binding site occupied with Cu^{+}. In both cases, the second Cu^{+} ion took alternative routes either into the protein (transient site occupied) or peripheral to the protein (internal site occupied). Because none of these alternative routes

involved interactions to the internal acceptor Cys382 (Table S2), our results suggest the entry and binding of one single Cu^+ ion.

Discussion

In this work, we characterized membrane anchoring and ion-entry into LpCopA, a prototypical Cu^+-transporting P-type ATPase from *Legionella pneumophila.* By combining computational and experimental techniques we characterized exposed charges on the docking platform (helix MB') and identified the location and chemical characteristics of one transient and one internal binding site, as well as the structural dynamics involved in our proposed ion-transfer mechanism. Thus, here we build on our recent characterization of the release mechanisms of Cu^+ (10) and Zn^{2+} (11) heavy-metal transporting P-type ATPases.

It is well established that biological membranes are not just inert matrices for membrane proteins, but rather should be viewed as allosteric modulators of protein function (60). For instance, protein-lipid interactions for the sugar transporter lactose permease (LacY) differ between phosphoethanolamine (PE) and phosphocholine (PC) lipids (61), which might explain the requirement for PE lipids (62, 63). Critical lipid dependencies have also been established for P-type ATPases. The Ca^{2+} transporting P-type ATPase SERCA1a is unstable in the absence of lipids (64), requires a ~30 Å thick lipid bilayer for optimal function (65, 66), and induces local deformations in the surrounding lipid bilayer (67). Likewise, the function of copper-transporting P-type ATPases is lipid-dependent since proteins solubilized in detergent are inactive in the absence of supplemented lipids (9, 68, 69). However, the molecular details governing lipid partitioning of Cu^+ ATPases have not been established.

Extracting structural information from simulations of membrane protein transporters requires a properly positioned TM domain. In this work, we explored the membrane anchoring of the Cu^+ ATPase using one of the existing crystal structures; the E2.P_i state (PDB ID: 3RFU), and the CHARMM36 force field, which have shown excellent agreement with experimental observables for the DOPC lipids (33). By measuring convergence of the protein position with respect to surrounding lipids in three MD simulations with different starting positions (Fig. S2), we established an atomistic structural description of LpCopA in the membrane (Fig. 1C). The simulated protein position closely resembled that obtained using the coarse-grained MemProtMD protocol (57). Because the OPM database (30) outputs the position of the two planes, one cannot expect a perfect agreement. Nevertheless, the predicted position of the periplasmic plane was close to our atomistic simulations, while there were larger discrepancies at the cytoplasmic side (Fig. S7B). Upon tracking protein-lipid interactions in the equilibrated part of the trajectories, a majority of the amino acids making close connections to the lipids were situated on the cytoplasmic side. Therefore, it is possible that a specific anchoring in the lipid bilayer is required for optimal function of Cu^+ ATPases, in particular on the cytoplasmic side where metallochaperones and/or the regulatory HMBD docks to deliver Cu^+ ions (24).

Positive charges on the MB' half-helix have been proposed to interact with Cu^+-carrying metallochaperones and/or HMBD (24). The MB' is oriented parallel to the membrane mediated by a double-glycine motif and have been identified as a putative docking platform for ion delivery (9). Interestingly, the simulated E2.P_i crystal structure underwent a rearrangement in the incline of helix MB' relative to the membrane (Fig. 3A), which may represent the optimal configuration of the CopA docking platform in the lipid interface. The starting configuration of the TM helices MA-MB and MB' represents those of the outward-facing E2P state and we do not claim our simulations to have reached

an E1 state. Rather, since the SERCA1a TM helices M7-M10 (70) and the beta and gamma subunits in the Na^+,K^+-ATPase (71) show very limited rearrangements in-between E2 and E1 states, the corresponding difference in the LpCopA MA-MB and MB' TM helices may also be characterized by similar restricted rearrangements in the E2-E1 transition. In that case, the three positively charged residues Lys135, Arg136, and Lys142 on helix MB' are likely solvated by water to a high extent throughout the reaction cycle, especially Arg136, which was almost exclusively exposed to water molecules (Fig. 3B).

To verify this finding, we mutated each of the three identified residues into a serine, which resulted in significantly reduced ATPase activity with the largest effects on Arg136 in an *in vitro* assay (Fig. 3C), in which added soluble cysteine has been shown to imitate the Cu^+ delivery of intracellular chaperones (68). The results from the *in vivo* assay only reported significant reduction of activity in the Lys142Ser single mutant. However, the activities of the Lys135Glu+Arg136Glu and Lys135Ser+Lys142Ser double mutants were drastically lowered compared to the wild-type protein. While the context of the biological assay is complex and we cannot fully explain the phenotypes associated with positions 135 and 136, it is clear that deleting positive charges has severe effects on protein activity. Together, these results corroborate with observations in AfCopA where deleting all positive charges on MB' prevented enzyme activation (24) and add a putative molecular explanation where the positive charges are exposed to solvent due to a highly flexible MB' platform. The importance of the Lys135, Arg136, Lys142 triplet is also reflected in the sequence conservation patterns. While none of the three residues belong to the invariant amino acids in the platform region, positive charges are very common in the MB' helix. In fact, in almost 90 % of ~1,700 sequences of Cu^+-transporting P_{IB}-ATPases, more than three (average 3.8) arginines, lysines or histidines are found in the short stretch from the double glycine

motif to Met148 at the intracellular beginning of TM1 (Table S3) (9). These residues are typically separated by three or four other residues, which suggest conserved charge directionality in the helix, almost certainly towards the intracellular side.

In AfCopA, it was shown that metallochaperones, rather than the HMBD, deliver Cu^+ (21). Since no metallochaperone specific to the LpCopA protein have yet been identified and the HMBD structure is atypical and unknown (72), we need to limit our study to characterization of a putative ion-entry path, i.e. subsequent to ion delivery. The differences between the AfCopA and LpCopA proteins have been reviewed in (14). The Met148, Glu205 and Asp337 triplet has been assigned a putative role as an ion entry site, which was proposed to provide Cu^+ to the internal ion-binding residues within the TM domain (9). In AfCopA, Ala mutants of the equivalent residues showed equal reduction in ATPase activity (24), but these experiments did not reveal how the ions are shuttled into the protein. Therefore, we monitored the dynamics of the putative entry site residues, first in the $E2.P_i$ crystal structure and then in an E1 model. In the $E2.P_i$ state, Met148 was observed to reorient toward the closest ion acceptor in the internal binding sites, Cys382, to a higher degree than Glu205 and Asp337 (Fig. 4A-B and Fig. S8). This is consistent with our *in vitro* data that showed the mutations Glu205Gln and Asp337Asn to have significantly less effect on LpCopA activity compared to the Met148Ala, Met148Cys, and Met148Ser mutations. The *in vivo* results suggested a less critical role for Asp337, while mutating Met148 or Glu205 resulted in significant loss of activity. This agrees with Asp337 being more distant to the proposed docking platform and suggests an alternative function for this residue, such as assisting chaperone/HMBD docking, while the more proximal Met148, and perhaps also Glu205, might be more directly involved in ion delivery to the TM domain.

The sulfur-sulfur distance between Met148 and the likely internal receiver Cys382 measures 9.3 Å in the Cu^+-free E2.P_i state crystal structure (9) and while both residues showed significant flexibility in the E2.P_i simulations, large-scale conformational changes are likely required to enable ion transfer, as observed in other P-type ATPase proteins (70). Therefore, while we so far relied on the accuracy of the crystal structure, to characterize a putative ion-entry mechanism we had to accept the possible uncertainties of modeling an inward-facing LpCopA E1 state. In addition, while the CHARMM36 force field is excellent for modeling atomistic lipid interactions that was essential to establish the lipid partitioning of LpCopA, it does not contain Cu^+ parameters. Parameterization of transition metal ions is a major effort and instead we shifted to the ffGromos53a6 force field (45), which proved a successful approach for determining structural dynamics and qualitative free energies associated with ion release from a Cu^+ ATPase. Still, the inherent difficulty in force field parameterization of metal ions should be acknowledged and other copper-protein models have been described (73, 74). Although much effort goes into developing polarizable force fields (75, 76), a complex membrane protein system is not the ideal test case and such force fields might introduce artificial effects that would be hard or impossible to detect. Nevertheless, our previous simulations show that it is possible to retrieve realistic results using non-polarizable force field parameters (10, 11). In addition, a Cu^+-bound E1 state high-resolution structure would add significantly to the understanding of the ion entry process and internal coordination. However, because such structures might not be amendable to structural characterization, alternative approaches combining biophysical and biochemical techniques enable mechanistic insight and identification of key residues and hence help decipher the molecular basis associated with membrane protein transport.

To introduce the ion into the protein interior, we applied a force on the Cu^+ ion towards the extracellular side with the aim of tracking the preferred pathway into the protein. The starting position of the ion is admittedly arbitrary. However, we do not claim to characterize ion delivery, but rather the entry path, and each time the ion entered the protein the exact same pathway was explored. In the simulation of the E1 state model, the average Met148-Cys382 sulfur-sulfur distance was significantly reduced and Met148 was observed to shuttle Cu^+ to Cys382, which assigns Met148 as main responsible for shuttling Cu^+ from the entry site. Two significant binding sites were identified in addition to the first transient Met148 contact (Site I in Fig. 5C); one near the cytoplasm between Met148 and Cys382 (Fig. 6A and Site II in Fig. 5C) and one internal with a trigonal coordination involving residues Cys384, Asn689, and Met717 (Fig. 6B and Site III in Fig. 5C). Recent X-ray absorption spectroscopy data suggested a partially exposed ion-binding site in the vicinity of Met148 (14), which corroborates with our observations. In addition, the X-ray absorption spectroscopy study assigned Cys382, Cys384 and Met717 to the internal binding site (14). The simulation data showed a similar trigonal coordination, but including Asn689 instead of Cys382, which could not be excluded from the EXAFS data (and is also supported by charge transfer measurements) (14). Our simulation rather assigns a relay point function to Cys382 to transiently coordinate the Cu^+ ion followed by shuttling to the internal binding site. Furthermore, in simulations where either of the two sites was occupied with a Cu^+ ion, a second ion failed to enter the proposed entry pathway. While this suggests a single-ion stoichiometry, we have not explored the effects of different cysteine protonation states that has been shown to affect Cu^+ uptake (77). Together, our results reconcile earlier experimental observations and offer a molecular view of the ion-entry process in Cu^+-transporting P-type ATPases.

Conclusion

Our work suggests that Cu^{+}-specific P-type ATPase membrane protein transporters anchor predominantly in cytoplasmic leaflet accompanied by subtle structural differences compared to available crystal structures that result in exposed positive charges on the putative MB' docking platform. The ion-entry molecular path is proposed to involve two ion-binding sites; one transient Met148-Cys382 site and one intramembranous site formed by trigonal coordination to Cys384, Asn689, and Met717, which provide a molecular understanding of ion entry in Cu^{+}-transporting P-type ATPases.

Author Contributions

C.G. and O.S. performed the activity assays, P.G., E.L. and M.A. designed the research, M.A. performed and analyzed the computational simulations and all authors wrote the manuscript.

Acknowledgements

We thank Profs. Poul Nissen and Stephen H. White for invaluable advice and discussions throughout this project. This work was funded by grants from Marie Curie Career Integration Grant (FP7-MC-CIG-618558), Magnus Bergvalls Stiftelse (2014-00170), Stiftelsen Olle Engkvist Byggmästare (2015/768), Åke Wibergs Stiftelse (M15-0148), and a Senior Postdoctoral Fellowship from the Branches Cost-Sharing Fund from the Institute of Complex Adaptive Matter ICAM supported in part by the National Science Foundation to Magnus Andersson, and the Swedish e-Science Research Center (SeRC), and the Swedish Research Council (2013-5901) to Erik Lindahl. The work was also supported by Lundbeck Foundation, Wallenberg Academy Fellowships, and a Project Research Grant for Junior Researchers to Pontus Gourdon, as well as by a NIH grant GM074637 to Stephen H. White, University of California at Irvine. Computational resources were provided by the Swedish National Infrastructure

for Computing (2014/11-33) and the U.S. National Science Foundation through TeraGrid (now Xsede) resources provided by the Texas Advanced Computing Center at the University of Texas at Austin.

References

1. Mattie, M. D., and J. H. Freedman. 2004. Copper-inducible transcription: regulation by metal- and oxidative stress-responsive pathways. Am. J. Physiol. Cell Physiol. 286:C293-301.
2. Prohaska, J. R. 2008. Role of copper transporters in copper homeostasis. Am. J. Clin. Nutr. 88:826S-829S.
3. Kehrer, J. P. 2000. The Haber-Weiss reaction and mechanisms of toxicity. Toxicology 149:43-50.
4. Jomova, K., and M. Valko. 2011. Advances in metal-induced oxidative stress and human disease. Toxicology 283:65-87.
5. Osman, D., and J. S. Cavet. 2008. Copper homeostasis in bacteria. Adv. Appl. Microbiol. 65:217-247.
6. Kaplan, J. H., and S. Lutsenko. 2009. Copper transport in mammalian cells: special care for a metal with special needs. J. Biol. Chem. 284:25461-25465.
7. Williams, L. E., and R. F. Mills. 2005. P(1B)-ATPases--an ancient family of transition metal pumps with diverse functions in plants. Trends Plant Sci. 10:491-502.
8. Gupta, A., and S. Lutsenko. 2009. Human copper transporters: mechanism, role in human diseases and therapeutic potential. Future Med. Chem. 1:1125-1142.
9. Gourdon, P., X.-Y. Liu, T. Skjørringe, J. P. Morth, L. B. Møller, B. P. Pedersen, and P. Nissen. 2011. Crystal structure of a copper-transporting PIB-type ATPase. Nature 475:59-64.
10. Andersson, M., D. Mattle, O. Sitsel, T. Klymchuk, A. M. Nielsen, L. B. Moller, S. H. White, P. Nissen, and P. Gourdon. 2014. Copper-transporting P-type ATPases use a unique ion-release pathway. Nat. Struct. Mol. Biol. 21:43-48.
11. Wang, K., O. Sitsel, G. Meloni, H. E. Autzen, M. Andersson, T. Klymchuk, A. M. Nielsen, D. C. Rees, P. Nissen, and P. Gourdon. 2014. Structure and mechanism of Zn2+-transporting P-type ATPases. Nature 514:518-522.
12. Arguello, J. M. 2003. Identification of ion-selectivity determinants in heavy-metal transport P1B-type ATPases. J. Membr. Biol. 195:93-108.
13. Raimunda, D., P. Subramanian, T. Stemmler, and J. M. Arguello. 2012. A tetrahedral coordination of Zinc during transmembrane transport by P-type Zn(2+)-ATPases. Biochim. Biophys. Acta 1818:1374-1377.
14. Mattle, D., L. Zhang, O. Sitsel, L. T. Pedersen, M. R. Moncelli, F. Tadini-Buoninsegni, P. Gourdon, D. C. Rees, P. Nissen, and G. Meloni. 2015. A sulfur-based transport pathway in Cu+-ATPases. EMBO reports 16:728-740.
15. Rosenzweig, A. C., and J. M. Arguello. 2012. Toward a molecular understanding of metal transport by P(1B)-type ATPases. Curr. Top. Membr. 69:113-136.
16. Gonzalez-Guerrero, M., E. Eren, S. Rawat, T. L. Stemmler, and J. M. Arguello. 2008. Structure of the two transmembrane Cu+ transport sites of the Cu+ -ATPases. J. Biol. Chem. 283:29753-29759.
17. Kuhlbrandt, W. 2004. Biology, structure and mechanism of P-type ATPases. Nat. Rev. Mol. Cell Biol. 5:282-295.
18. Post, R. L., C. Hegyvary, and S. Kume. 1972. Activation by adenosine triphosphate in the phosphorylation kinetics of sodium and potassium ion transport adenosine triphosphatase. J. Biol. Chem. 247:6530-6540.
19. Albers, R. W. 1967. Biochemical aspects of active transport. Annu. Rev. Biochem 36:727-756.

20. Bublitz, M., H. Poulsen, J. P. Morth, and P. Nissen. 2010. In and out of the cation pumps: P-type ATPase structure revisited. Curr. Opin. Struct. Biol. 20:431-439.
21. Gonzalez-Guerrero, M., and J. M. Arguello. 2008. Mechanism of Cu+-transporting ATPases: soluble Cu+ chaperones directly transfer Cu+ to transmembrane transport sites. Proc. Natl. Acad. Sci. U. S. A. 105:5992-5997.
22. Mitra, B., and R. Sharma. 2001. The cysteine-rich amino-terminal domain of ZntA, a Pb(II)/Zn(II)/Cd(II)-translocating ATPase from Escherichia coli, is not essential for its function. Biochemistry 40:7694-7699.
23. O'Halloran, T. V., and V. C. Culotta. 2000. Metallochaperones, an intracellular shuttle service for metal ions. J. Biol. Chem. 275:25057-25060.
24. Padilla-Benavides, T., C. J. McCann, and J. M. Arguello. 2013. The mechanism of Cu+ transport ATPases: interaction with CU+ chaperones and the role of transient metal-binding sites. J. Biol. Chem. 288:69-78.
25. Winther, A. M., M. Bublitz, J. L. Karlsen, J. V. Moller, J. B. Hansen, P. Nissen, and M. J. Buch-Pedersen. 2013. The sarcolipin-bound calcium pump stabilizes calcium sites exposed to the cytoplasm. Nature 495:265-269.
26. Toyoshima, C., M. Nakasako, H. Nomura, and H. Ogawa. 2000. Crystal structure of the calcium pump of sarcoplasmic reticulum at 2.6 A resolution. Nature 405:647-655.
27. Jensen, A. M., T. L. Sorensen, C. Olesen, J. V. Moller, and P. Nissen. 2006. Modulatory and catalytic modes of ATP binding by the calcium pump. EMBO J. 25:2305-2314.
28. Blaby-Haas, C. E., T. Padilla-Benavides, R. Stube, J. M. Arguello, and S. S. Merchant. 2014. Evolution of a plant-specific copper chaperone family for chloroplast copper homeostasis. Proc. Natl. Acad. Sci. U. S. A. 111:E5480-5487.
29. Jo, S., J. B. Lim, J. B. Klauda, and W. Im. 2009. CHARMM-GUI Membrane Builder for mixed bilayers and its application to yeast membranes. Biophys. J. 97:50-58.
30. Lomize, M. A., A. L. Lomize, I. D. Pogozheva, and H. I. Mosberg. 2006. OPM: orientations of proteins in membranes database. Bioinformatics 22:623-625.
31. Phillips, J. C., R. Braun, W. Wang, J. Gumbart, E. Tajkhorshid, E. Villa, C. Chipot, R. D. Skeel, L. Kale, and K. Schulten. 2005. Scalable molecular dynamics with NAMD. J. Comput. Chem. 26:1781-1802.
32. Mackerell, A. D., Jr., M. Feig, and C. L. Brooks, 3rd. 2004. Extending the treatment of backbone energetics in protein force fields: limitations of gas-phase quantum mechanics in reproducing protein conformational distributions in molecular dynamics simulations. J. Comput. Chem. 25:1400-1415.
33. Klauda, J. B., R. M. Venable, J. A. Freites, J. W. O'Connor, D. J. Tobias, C. Mondragon-Ramirez, I. Vorobyov, A. D. MacKerell, Jr., and R. W. Pastor. 2010. Update of the CHARMM all-atom additive force field for lipids: validation on six lipid types. J. Phys. Chem. B 114:7830-7843.
34. Jorgensen, W., J. Chandrasekhar, J. Madura, R. Impey, and M. Klein. 1983. Comparison of simple potential functions for simulating liquid water. J. Chem. Phys. 79:926-935.
35. Best, R. B., X. Zhu, J. Shim, P. E. Lopes, J. Mittal, M. Feig, and A. D. Mackerell, Jr. 2012. Optimization of the additive CHARMM all-atom protein force field targeting improved sampling of the backbone phi, psi and side-chain chi(1) and chi(2) dihedral angles. J. Chem. Theory Comput. 8:3257-3273.

36. Darden, T., D. York, and L. Pedersen. 1993. Particle mesh Ewald: An N·log(N) method for Ewald sums in large systems. J. Chem. Phys. 98:10089-10092.
37. Essmann, U., L. Perera, M. Berkowitz, T. Darden, H. Lee, and L. Pedersen. 1995. A smooth particle mesh Ewald method. J. Chem. Phys. 103:8577-8593.
38. Ryckaert, J.-P., G. Ciccotti, and H. Berendsen. 1977. Numerical integration of the cartesian equations of motion of a system with constraints: molecular dynamics of n-alkanes. J. Comput. Phys. 23:327-341.
39. Miyamoto, S., and P. Kollman. 1992. Settle: An analytical version of the SHAKE and RATTLE algorithm for rigid water models. J. Comput. Chem. 13:952-962.
40. Feller, S., Y. Zhang, R. Pastor, and B. Brooks. 1995. Constant pressure molecular dynamics simulation: The Langevin piston method. J. Chem. Phys. 103:4613-4621.
41. Martyna, G., D. Tobias, and M. Klein. 1994. Constant pressure molecular dynamics algorithms. J. Chem. Phys. 101:4177-4189.
42. Palmgren, M. G., and P. Nissen. 2011. P-type ATPases. Annual review of biophysics 40:243-266.
43. Emsley, P., B. Lohkamp, W. G. Scott, and K. Cowtan. 2010. Features and development of Coot. Acta Crystallogr. D Biol. Crystallogr. 66:486-501.
44. Krissinel, E., and K. Henrick. 2004. Secondary-structure matching (SSM), a new tool for fast protein structure alignment in three dimensions. Acta Crystallogr. D Biol. Crystallogr. 60:2256-2268.
45. Oostenbrink, C., A. Villa, A. E. Mark, and W. F. van Gunsteren. 2004. A biomolecular force field based on the free enthalpy of hydration and solvation: the GROMOS force-field parameter sets 53A5 and 53A6. J. Comput. Chem. 25:1656-1676.
46. Berendsen, H. J. C., J. P. M. Postma, W. F. von Gunstaren, and J. Hermans. 1981. Intermolecular Forces (Jerusalem Symposia). Springer.
47. Hess, B., C. Kutzner, D. van der Spoel, and E. Lindahl. 2008. GROMACS 4: Algorithms for Highly Efficient, Load-Balanced, and Scalable Molecular Simulation. J. Chem. Theory Comput. 4:435-447.
48. Nosé, S. 1984. A unified formulation of the constant temperature molecular dynamics methods. J. Chem. Phys. 81:511-519.
49. Hoover, W. 1985. Canonical dynamics: Equilibrium phase-space distributions. Phys. Rev. A 31:1695-1697.
50. Nosé, S., and M. L. Klein. 1983. Constant pressure molecular dynamics for molecular systems. Mol. Phys. 50:1055-1076.
51. Parrinello, M., and A. Rahman. 1981. Polymorphic transitions in single crystals: A new molecular dynamics method. J. Appl. Phys. 52:7182-7190.
52. Hess, B., H. Bekker, H. Berendsen, and J. Fraaije. 1997. LINCS: A linear constraint solver for molecular simulations. J. Comput. Chem. 18:1463-1472.
53. Humphrey, W., A. Dalke, and K. Schulten. 1996. VMD: visual molecular dynamics. J. Mol. Graph. 14:33-38, 27-38.
54. Baginski, E. S., P. P. Foa, and B. Zak. 1967. Microdetermination of inorganic phosphate, phospholipids, and total phosphate in biologic materials. Clin. Chem. 13:326-332.
55. Schneider, C. A., W. S. Rasband, and K. W. Eliceiri. 2012. NIH Image to ImageJ: 25 years of image analysis. Nat. Methods 9:671-675.

56. Petersen, C., and L. B. Moller. 2000. Control of copper homeostasis in Escherichia coli by a P-type ATPase, CopA, and a MerR-like transcriptional activator, CopR. Gene 261:289-298.
57. Stansfeld, P. J., J. E. Goose, M. Caffrey, E. P. Carpenter, J. L. Parker, S. Newstead, and M. S. Sansom. 2015. MemProtMD: Automated Insertion of Membrane Protein Structures into Explicit Lipid Membranes. Structure 23:1350-1361.
58. Andersson, M., J. A. Freites, D. J. Tobias, and S. H. White. 2011. Structural dynamics of the S4 voltage-sensor helix in lipid bilayers lacking phosphate groups. J. Phys. Chem. B 115:8732-8738.
59. Olesen, C., M. Picard, A. M. Winther, C. Gyrup, J. P. Morth, C. Oxvig, J. V. Moller, and P. Nissen. 2007. The structural basis of calcium transport by the calcium pump. Nature 450:1036-1042.
60. Lee, A. G. 2004. How lipids affect the activities of integral membrane proteins. Biochim. Biophys. Acta 1666:62-87.
61. Andersson, M., A. N. Bondar, J. A. Freites, D. J. Tobias, H. R. Kaback, and S. H. White. 2012. Proton-coupled dynamics in lactose permease. Structure 20:1893-1904.
62. Bogdanov, M., P. N. Heacock, and W. Dowhan. 2002. A polytopic membrane protein displays a reversible topology dependent on membrane lipid composition. EMBO J. 21:2107-2116.
63. Bogdanov, M., P. Heacock, Z. Guan, and W. Dowhan. 2010. Plasticity of lipid-protein interactions in the function and topogenesis of the membrane protein lactose permease from Escherichia coli. Proc. Natl. Acad. Sci. U. S. A. 107:15057-15062.
64. Lund, S., S. Orlowski, B. de Foresta, P. Champeil, M. le Maire, and J. V. Moller. 1989. Detergent structure and associated lipid as determinants in the stabilization of solubilized Ca2+-ATPase from sarcoplasmic reticulum. J. Biol. Chem. 264:4907-4915.
65. Starling, A. P., J. M. East, and A. G. Lee. 1993. Effects of phosphatidylcholine fatty acyl chain length on calcium binding and other functions of the (Ca(2+)-Mg2+)-ATPase. Biochemistry 32:1593-1600.
66. Caffrey, M., and G. W. Feigenson. 1981. Fluorescence quenching in model membranes. 3. Relationship between calcium adenosinetriphosphatase enzyme activity and the affinity of the protein for phosphatidylcholines with different acyl chain characteristics. Biochemistry 20:1949-1961.
67. Sonntag, Y., M. Musgaard, C. Olesen, B. Schiott, J. V. Moller, P. Nissen, and L. Thogersen. 2011. Mutual adaptation of a membrane protein and its lipid bilayer during conformational changes. Nat. Commun. 2:304.
68. Yang, Y., A. K. Mandal, L. M. Bredeston, F. L. Gonzalez-Flecha, and J. M. Arguello. 2007. Activation of Archaeoglobus fulgidus Cu(+)-ATPase CopA by cysteine. Biochim. Biophys. Acta 1768:495-501.
69. Chintalapati, S., R. Al Kurdi, A. C. van Scheltinga, and W. Kuhlbrandt. 2008. Membrane structure of CtrA3, a copper-transporting P-type-ATPase from Aquifex aeolicus. J. Mol. Biol. 378:581-595.
70. Moller, J. V., C. Olesen, A. M. Winther, and P. Nissen. 2010. The sarcoplasmic Ca2+-ATPase: design of a perfect chemi-osmotic pump. Q. Rev. Biophys. 43:501-566.
71. Nyblom, M., H. Poulsen, P. Gourdon, L. Reinhard, M. Andersson, E. Lindahl, N. Fedosova, and P. Nissen. 2013. Crystal structure of Na+, K(+)-ATPase in the Na(+)-bound state. Science 342:123-127.

72. Sitsel, O., C. Gronberg, H. E. Autzen, K. Wang, G. Meloni, P. Nissen, and P. Gourdon. 2015. Structure and Function of Cu(I)- and Zn(II)-ATPases. Biochemistry 54:5673-5683.
73. Click, T. H., S. Y. Ponomarev, and G. A. Kaminski. 2012. Importance of electrostatic polarizability in calculating cysteine acidity constants and copper(I) binding energy of Bacillus subtilis CopZ. J. Comput. Chem. 33:1142-1151.
74. Ponomarev, S. Y., T. H. Click, and G. A. Kaminski. 2011. Electrostatic polarization is crucial in reproducing Cu(I) interaction energies and hydration. J. Phys. Chem. B 115:10079-10085.
75. Yu, H., and W. van Gunsteren. 2005. Accounting for polarization in molecular simulation. Comput. Phys. Commun. 172:69-85.
76. Lopes, P., B. Roux, and A. MacKerell. 2009. Molecular modeling and dynamics studies with explicit inclusion of electronic polarizability. Theory and applications. Theor. Chem. Acc. 124:11-28.
77. Dumay, Q. C., A. J. Debut, N. M. Mansour, and M. H. Saier, Jr. 2006. The copper transporter (Ctr) family of Cu+ uptake systems. J. Mol. Microbiol. Biotechnol. 11:10-19.

SUPPORTING INFORMATION

Membrane anchoring and ion-entry dynamics in a copper-transporting P-type ATPase

C. Grønberg, O. Sitsel, E. Lindahl, P. Gourdon, and M. Andersson

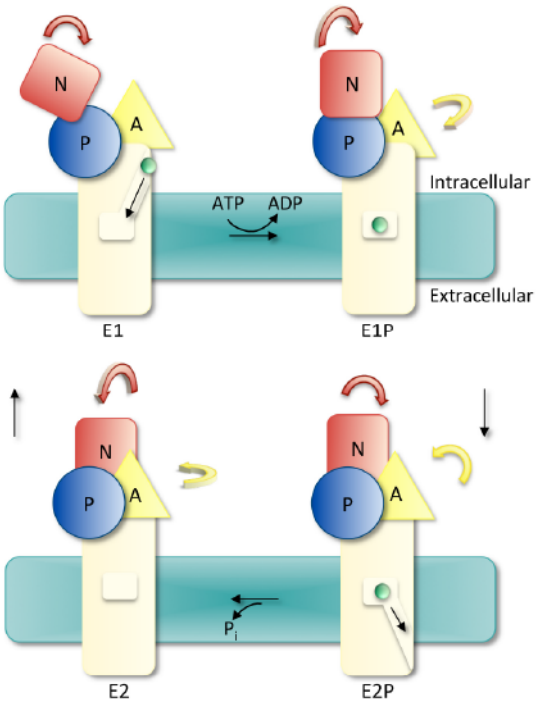

Figure S1. A schematic illustrating the overall E1-E1P-E2P-E2 reaction scheme. The cytosolic domains are shown as in Figure 1 and copper is depicted in green.

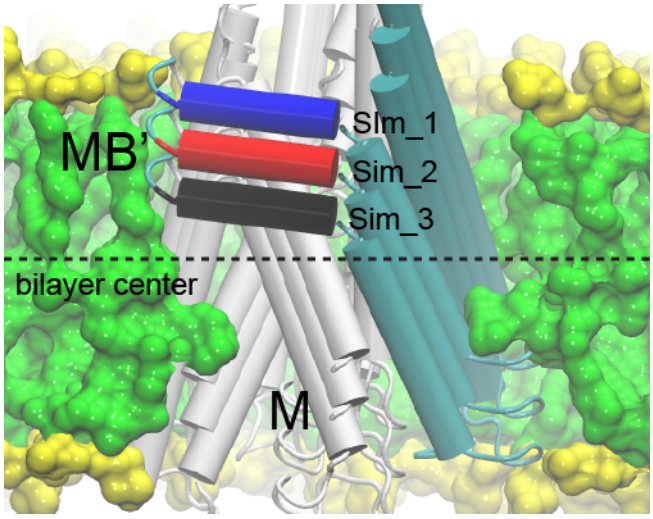

Figure S2. Simulation-system setup. The initial positions of LpCopA relative to the lipid bilayer are shown using different colors for the MB' platform; red for the system that was aligned according to the "Orientations of Proteins in Membranes" (OPM) database (Sim_2), and black and blue for systems inserted 5 Å below (Sim_1) and above (Sim_3) the aligned position.

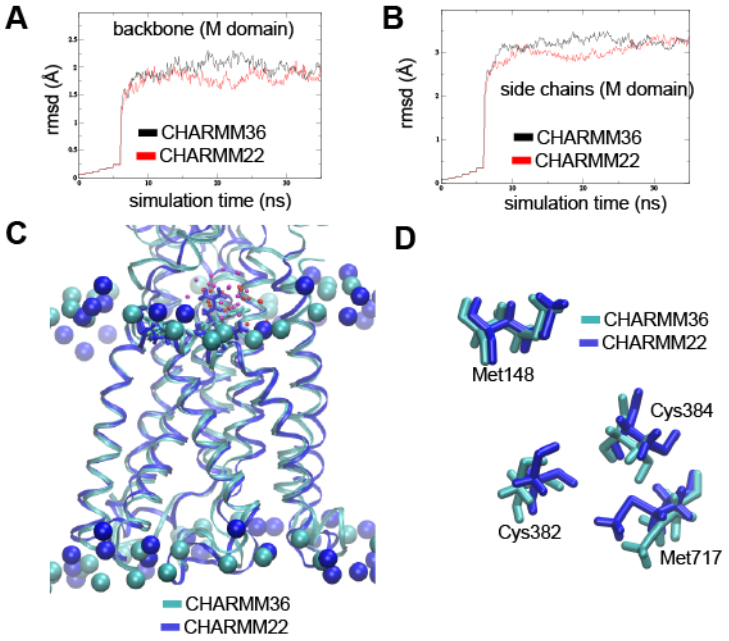

Figure S3. Comparison of simulation dynamics between CHARMM22 and CHARMM36 protein force fields. **(A)** Backbone and **(B)** Side-chain rmsd for the M domain obtained by CHARMM22 (red) and CHARMM36 (black) force fields, respectively. **(C)** Superimposed M domain protein structures corresponding to 35 ns of simulation with the CHARMM22 (blue) and CHARMM36 (cyan) force fields. The proteins are shown in ribbon representation and lipid phosphates are shown as vdW spheres. Platform residues Lys135, Arg136, and Lys142 are shown in licorice and waters within 4 Å from the platform residues are shown in red (CHARMM22) and magenta (CHARMM36). **(D)** Superimposed critical amino acid residues corresponding to 35 ns of simulation with the CHARMM22 (blue) and CHARMM36 (cyan) force field, respectively.

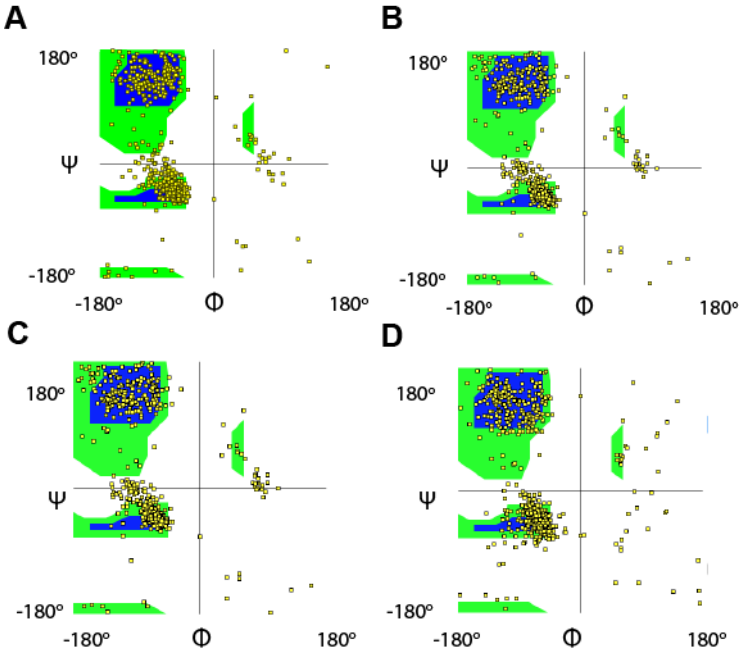

Figure S4. Structural integrity of the E1 model. Ramachandran plots of the **(A)** E2P crystal structure (PDB ID: 4BBJ), **(B)** the E1 model after 10 ns of CHARMM equilibration, **(C)** before and **(D)** after the pull simulation.

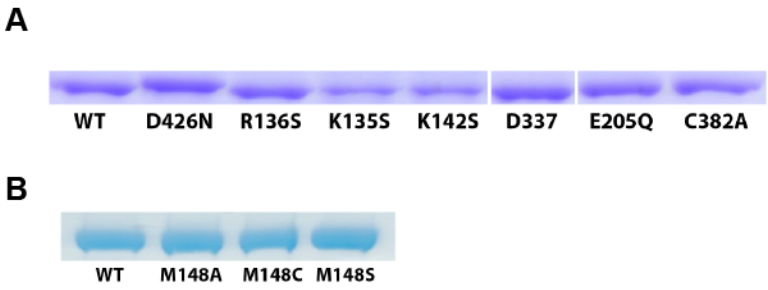

Figure S5. Control SDS-PAGE displaying relative protein concentrations in the *in vitro* functional assays of **(A)** R136S, K135S, K142S, D337N, E205Q, C382A, and **(D)** M148A, M148C, and M148S.

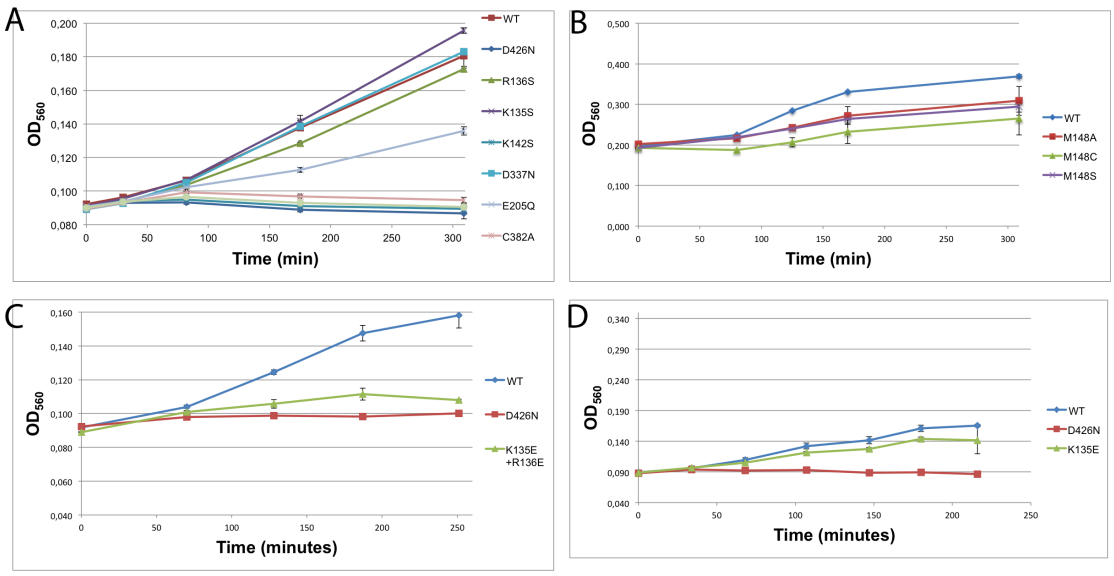

Figure S6. *In vivo* functional assays. Growth curves of wild-type and mutant LpCopA **(A)** D426N, R136S, K135S, K142S, D337N, E205Q, C382A **(B)** M148A, M148C, M148S **(C)** D426N, K135E+R136E **(D)** D426N, K135E in supplemented *E. coli* cells deficient in native CopA. The $CuCl_2$ concentration was 3.5 mM.

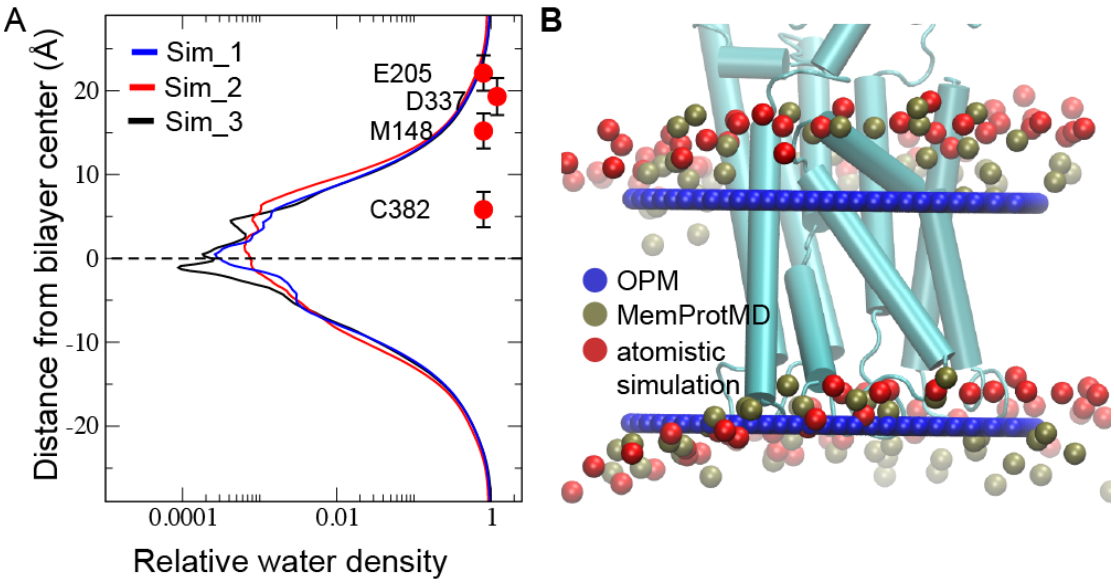

Figure S7. (A) The water density profiles for the converged part (>150 ns) of the three simulations and merged COM for the putative entry site triplet (Met148, Glu205 and Asp337) and internal site residue (Cys382). **(B)** Comparison of membrane insertion of LpCopA (cyan) using the "Orientations of Proteins in Membranes" (OPM) database (blue vDW patches), the MemProtMD database (lipid phosphates show in brown), and our atomistic simulation approach (lipid phosphates shown in red).

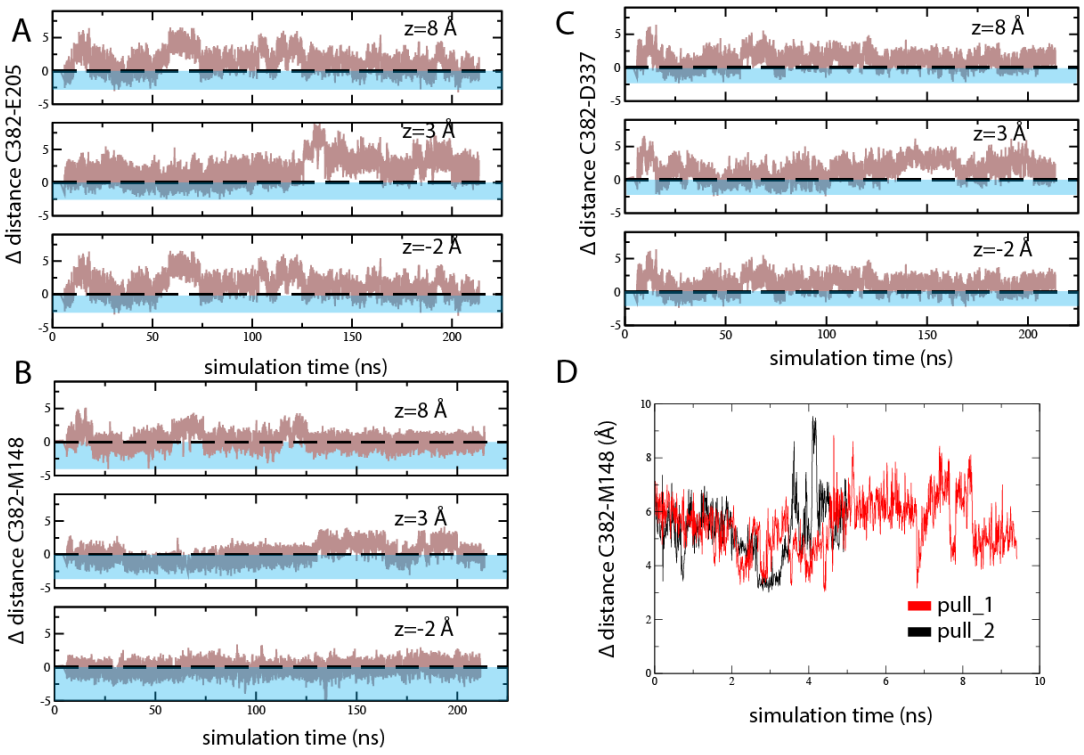

Figure S8. Inter-residue distances between Cys382 and **(A)** Glu205, **(B)** Met148, **(C)** Asp337 relative to the crystal structure distances (zero, dashed lines) for the three simulations; Sim_1, Sim_2, and Sim_3. The blue sections denote the distance range < crystal structure distance. **(D)** Inter-residue distances between Cys382 and Met148 in the simulations of the E1 state in the presence of Cu^{+}.

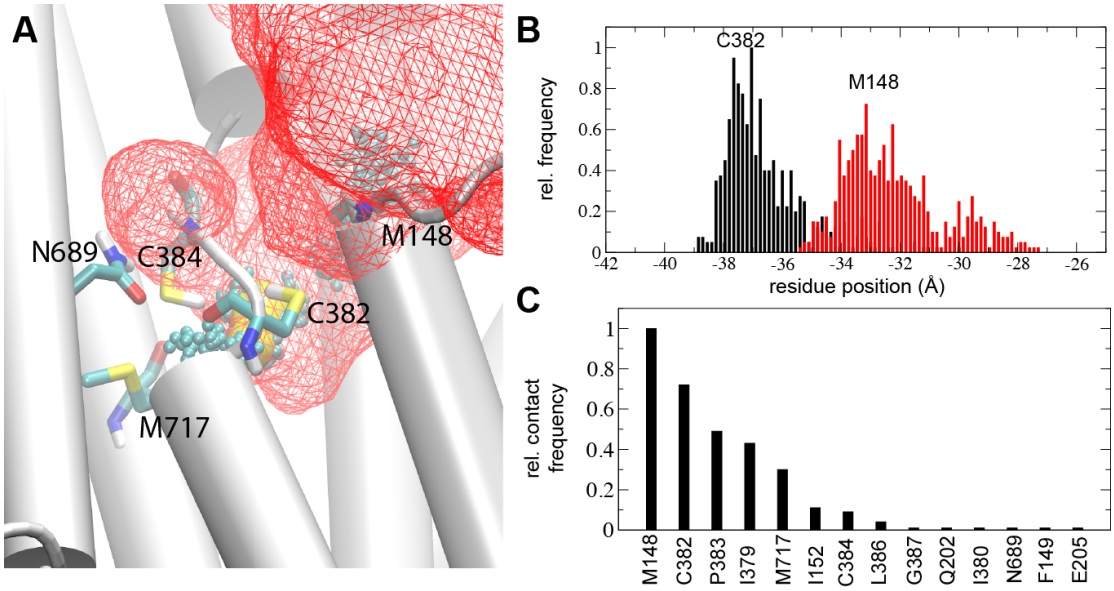

Figure S9. Water and Cu^{+} dynamics. **(A)** Water molecules within 10 Å of Met148 extracted from the 100 ns gromos simulation are shown as a red mesh isodensity surface at 5 % occupancy. **(B)** Structural rearrangements of Met148 and Cys382 side chains in the presence of Cu^{+} depicted as center-of-mass (COM) fluctuations in the pull_2 simulation. **(B)** Contact analysis showing the relative number of instances the Cu^{+} was < 3.5 Å from any protein residue during the pull_2 simulation.

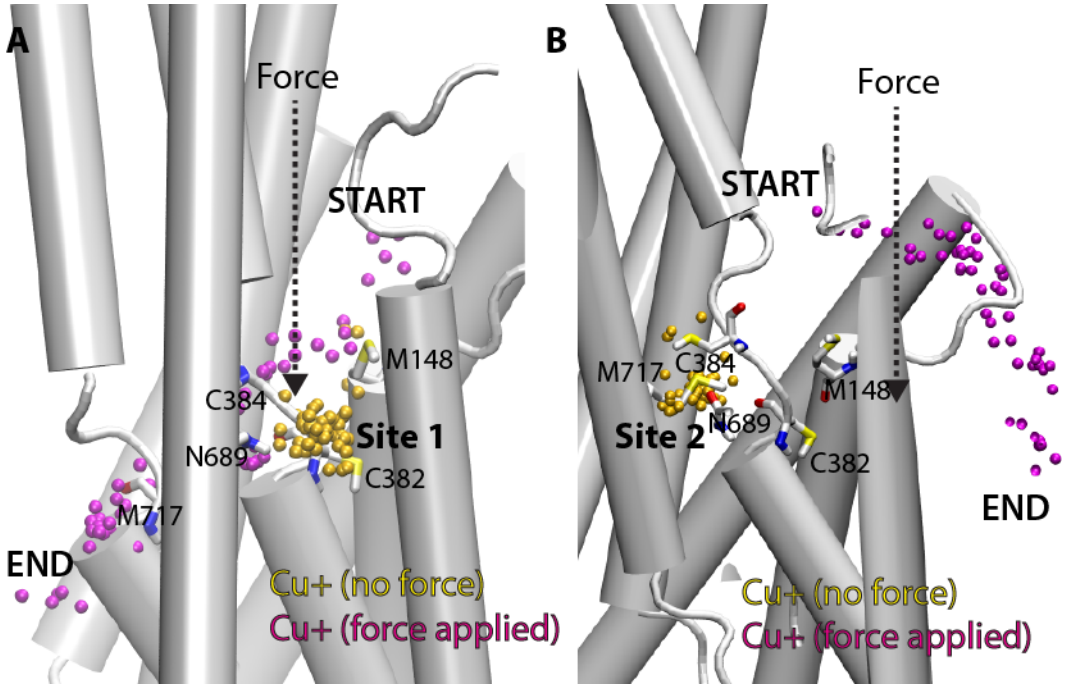

Figure S10. Simulations addressing a putative two-ion Cu^{+} entry. **(A)** A Cu^{+} ion with a starting position in-between residues Met148 and Cys382 (Site 1) was simulated without applied external force (yellow). A starting position for the second Cu^{+} ion (magenta) was chosen vertically aligned to the primary entry site residue Met148 and an external force was applied throughout the simulation. The ion positions correspond to every 1250 ps in a 25000 ps trajectory. **(B)** Similar setup as in (A) with the nonbiased Cu^{+} ion in a starting position proximal to Cys382, Asn689 and Met717 (Site 2).

Simulation	Trajectory lenght (ns)	C382 position along membrane vertical (Å)	M148 position along membrane vertical (Å)	M148-C382 distance (Å)
apo (Sim_1)	210	-36±2	-27±1	9±2
apo (Sim_2)	210	-34±2	-25±2	9±2
apo (Sim_3)	210	-32±2	-23±2	9±2
Cu^+ pull_1 1.25Å/ns	10	-36±1	-31±1	5±1
Cu^+ pull_2 2.5 Å/ns	5	-37±1	-32±1	5±1

Table S1. Simulation lengths, center-of-mass positions of residues Cys382 and Met148, and the corresponding Met148-Cys382 distance.

Simulation (Transient Site occupied)		**Simulation (Internal site occupied)**	
Residue	**Contact time (ns)**	**Residue**	**Contact time (ns)**
Met717	4.28	**Gly144**	3.81
Cys384	3.25	**Thr143**	3.11
Glu205	2.45	**Gln145**	1.30
Phe149	1.99	**Leu146**	0.28
Pro383	1.04	**Asn147**	0.13
Ala714	0.99	**Ser340**	0.8
Leu386	0.88	**Ser140**	0.7
Asn147	0.66	**Leu386**	0.6
Ala718	0.64	**Arg334**	0.3
Gly387	0.62	**Leu335**	0.2

Table S2. Residues within 3.5 Å and contact times of a second docking Cu^{+} during 10 ns steered MD simulations with either the transient Cu^{+} site or the internal Cu^{+} binding site occupied.

Number of Lys and Arg in MB'	Number of sequences
0	1
1	16
2	172
3	265
4	126
5	34
6	3
7	0

Table S3. Number of positively charged residues in the MB' helix of 617 CopA-type proteins with less than 95 % sequence identity selected from the UniProt database were included in the analysis.